J Mater Sci (2008) 43:3351–3363
DOI 10.1007/s10853-008-2549-6

Analysis of fracture limit curves and void coalescence in high strength interstitial free steel sheets formed under different stress conditions

R. Narayanasamy · N. L. Parthasarathi · R. Ravindran · C. Sathiya Narayanan

Received: 10 May 2007 / Accepted: 11 February 2008 / Published online: 22 March 2008

Abstract Void formation, which is a statistical event, depends on inhomogeneities present in the microstructure. The analysis on void nucleation, their growth and coalescence during the fracture of high strength interstitial free steel sheets of different thicknesses is presented in this article. The analysis shows that the criterion of void coalescence depends on the d-factor, which is the ratio of relative spacing of the ligaments (δd) present between the two consecutive voids to the radius of the voids. The computation of hydrostatic stress (σ_m), the dominant factor in depicting the evolution of void nucleation, growth and coalescence and the dimensional analysis of three different types of voids namely oblate, prolate and spherical type, have been carried out. The ratio of the length to the width (L/W) of the oblate or prolate voids at fracture is correlated with the mechanical properties, microstructure, strains at fracture, Mohr's circle shear strains and Triaxiality factors. The Lode angle (θ) is determined and correlated with the stress triaxiality factor (T), ratio of mean stress (σ_m) to effective stress (σ_e). In addition, the Void area fraction (V_a), which is the ratio of void area to the representative area, is determined and correlated with the strain triaxiality factor (T_o).

R. Narayanasamy (✉) · N. L. Parthasarathi · R. Ravindran · C. S. Narayanan
Department of Production Engineering, National Institute of Technology, Tiruchirappalli 620015, TN, India
e-mail: narayan@nitt.edu

N. L. Parthasarathi
e-mail: nlpartha@nitt.edu

R. Ravindran
e-mail: mceravindran@yahoo.co.in

C. S. Narayanan
e-mail: csathiyanarayanan@yahoo.co.in

Nomenclature

ε_1	Major strain
ε_2	Minor strain
ε_3	Thickness strain
ε_e	Effective strain of macroscopic equivalent strain
ε_m	Hydrostatic or mean strain
γ_{12}, γ_{23}, γ_{13}	Mohr's circle shear strains (the subscripts 1, 2 & 3 represent major, minor and thickness strains)
δd	Ligament thickness
d-factor/ ratio	Ratio of δd to radius of void
θ	Lode factor or lode angle
T	Stress triaxiality factor or ratio
T_0	Stress triaxiality factor or ratio
σ_e	Effective stress
σ_m	Mean or hydrostatic stress
V_a	Void area fraction

Introduction

In any material, fracture (the final phase failure) occurs due to the nucleation, growth and coalescence of voids formed after the onset of necking. Therefore the nucleation, growth and coalescence of voids influence the fracture behaviour of any material. Many researchers have investigated the nucleation, growth and coalescence of voids in porous materials as given below. Gurson and Tvergaard assumed

the voids are spherical in materials and remain spherical in growth [1], but many engineering materials have non-spherical voids. Later, Needleman found critical void volume fraction (f_c), which was often used to designate the final material failure [2]. Then, Gologanu et al. [3–5] derived a yield function for materials containing spherical voids overcoming the GT Model. However, Benzerga explained that the fracture is strongly influenced by void shape, void spacing, stress triaxiality and strain hardening [6]. Pardoen and Hutchinson, Benzerga and Kim implemented the GLD models to predict ductile material criteria [7–9]. Further, Stress triaxiality factor [T] was found to be a parameter to characterize the effect of triaxial stress state on ductile fracture which is responsible for the nucleation of voids. However, multiple stress states with different principal stress values can result in the same stress triaxiality factor, which is explained elsewhere [10]. Gao et al. [11], found the macroscopic stress response, void growth and coalescence behaviour during fracture. Recently, it is further confirmed that the metals have initially spherical voids and the void shape may change to prolate or oblate depending upon the state of applied stress [12]. From the above literature, it is found that d-factor, δd-factor, hydrostatic stress (σ_m), microstructure, strains at fracture, Triaxiality factors, the Lode angle (θ), effective strain (σ_e) and Void area fraction (V_a) have an effect on ductile fracture behaviour. Moreover, the nucleation, growth and coalescence of voids find different pattern in porous materials and sheet metals. Failure criteria of the sheet material can be expressed as a function of stress triaxiality parameter (T) and the Lode angle (θ) [12]. On the other hand, standard test for formability of sheet metals has been developed [13–15] and many improvements have been made. In this work, formability of high strength interstitial free steel sheets have been assessed by constructing experimental FLD for these sheets and an attempt to establish the relationship among the above-said parameters and formability was also made.

Experimental work

The chemical composition and microstructure of steels considered for the study were observed as per the standard procedures and shown in the Table 1 and Fig. 1, respectively. The tensile properties of the sheets were determined using tensile test in Hounsfield Tensometer [14] and the same is presented in Table 2. To vary the strain conditions and to study the void formation under these different conditions, sheet samples of different widths were formed up to fracture, using a double action hydraulic press of capacity 2000 kN with standard die and punch set up which is used for formability tests. Prior to forming, circular grids in rectangular array were printed in the surface of the sheet blanks. As the blanks are formed, these circles became elliptical. The major diameter and minor diameter of these ellipses were used to measure the major strain (ε_1) and minor strain (ε_2). The formulae used to calculate these strains are given as follows.

$$\text{major strain } (\varepsilon_1) = \ln(\text{major diameter of the ellipse/original diameter of the circle})$$

$$\text{minor strain } (\varepsilon_2) = \ln(\text{minor diameter of the ellipse/original diameter of the circle})$$

The thickness of the sheet in different locations was measured using a coordinate measuring machine (CMM) and thickness strain was calculated using the expression

$$\text{Thickness strain } (\varepsilon_3) = \ln(\text{thickness after forming/original thickness})$$

All these strains (ε_1,ε_2 and ε_3) were measured in necked, fractured and safe region.

Using strain measurements, the Forming and Fracture Limit Diagrams were drawn. From these strain-based limit diagrams, the stress-based forming and fracture limit diagrams were constructed [15]. Small sheet specimens of size 10 mm × 5 mm were cut at the region of fracture and fractured surfaces were observed for voids using a Scanning Electron Microscope (SEM) model JSM-5610LV for fractography analysis. By importing the SEM images to AutoCAD, the size and shape of voids were observed. From SEM images, the relative spacing of the ligaments (δd) present between the two consecutive voids was also measured from the fractography. The perimeters of the spherical voids were measured from SEM images

Table 1 Chemical composition of SPRC-35 high strength IF steels (in wt%)

Material	Thickness (mm)	C	Mn	Si	S	P	Al	Ti	B
SPRC-35 (High strength IF steel)	1.2	0.0027	0.43	0.008	0.010	0.048	0.050	0.004	0.0006
SPRC-35 (High strength IF steel)	1.0	0.0035	0.38	0.009	0.110	0.044	0.034	0.040	0.0006
SPRC-35 (High strength IF steel)	0.72	0.0027	0.40	0.012	0.009	0.046	0.033	0.045	0.0010

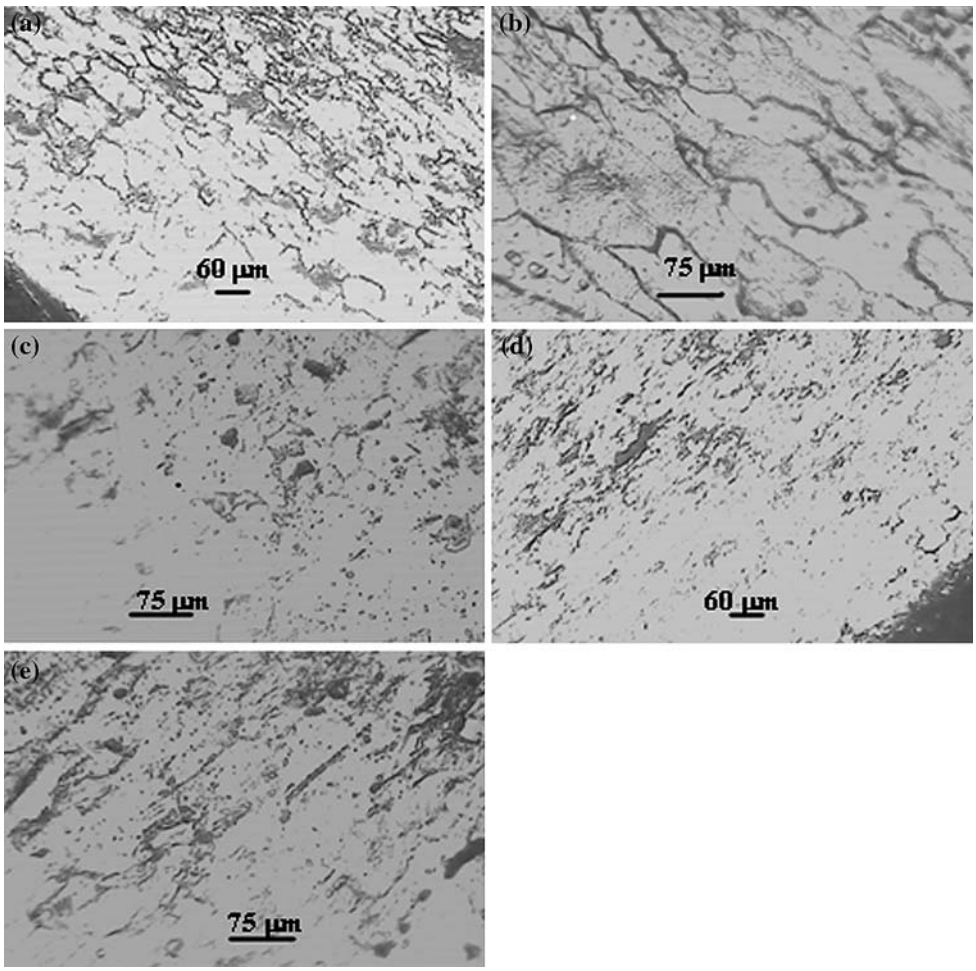

Fig. 1 Microstructure of SPRC high strength IF steel: (**a**) (thickness = 0.72 mm) at 250X; (**b**) (thickness = 0.72 mm) at 4000X; (**c**) (thickness = 1.00 mm) at 400X; (**d**) (thickness = 1.20 mm) at 250X; (**e**) (thickness = 1.20 mm) at 400X

Table 2 Tensile properties of SPRC-35 high strength IF steel of 0.72-mm thickness

Orientation relative to rolling direction	Strain hardening exponent n	Strength coefficient K (MPa)	Yield stress (σ_y) (MPa)	Ultimate tensile stress in MPa	UTS/σ_y	%Elongation
0°	0.2742	360	142	293	2.42	32.92
45°	0.1673	320	Average	Average		
90°	0.3369	540				
Average[a]	0.2364	385				

[a] Average = $(X_0 + 2X_{45} + X_{90})/4$, where X is n-value or K-value

and the average radii of the voids were found out. The d-factor was then determined by dividing the relative spacing of the ligaments (δd) present between the two consecutive voids by the radius of the voids. For the prolate and oblate voids, the length and width of the voids were measured from the SEM images and then the length to width ratio (L/W) of the voids was calculated. A representative material area (RMA) was chosen and the total area of the voids present in this particular RMA was calculated. From these data, the void area fraction, ratio of total area of the voids to the RMA was calculated. From the major strain, minor strain and thickness strain values, the Mohr's circle shear strains, macroscopic equivalent strain (ε_e), hydrostatic or mean strain (ε_m) and the Lode angle (θ),were determined as given in the Appendix 1. The strain triaxiality parameter was then calculated by dividing the macroscopic equivalent strain (ε_e) by hydrostatic strain (ε_m). The hydrostatic stress and macroscopic equivalent stress were also determined as explained in Appendix 1 and then the stress triaxiality

parameter was determined by dividing hydrostatic stress by macroscopic equivalent stress.

Results and discussion

Chemical composition and microstructure

The sheet having 0.72-mm thickness has comparatively more amount of silicon, which increases the strength of steels and has only traces of P and S, which decrease the elongation considerably. The sheet having 1.00-mm thickness has comparatively more amount of carbon (in ppm level), which increases the strength of the steel and also a small amount of Ti and B, which are carbide and nitride formers. The sheet having 1.20-mm thickness has comparatively more amount of manganese which contributes markedly to strength and hardness but to a lesser degree than carbon. It particularly counteracts the brittleness from sulphur and improves the formability. In these sheets, the high strength is derived from the precipitation of carbides, nitrides and sulphides and their compounds by alloying elements and pinning down of grain boundaries.

The microstructure of steel sheet having 1.20-mm thickness contains very fine pancake type of elongated ferrites and the lowest amount of carbides. The 0.72-mm-thick sheet contains coarse grains of ferrite and the highest amount of carbides. The increasing amount of carbides reduces the formability of steels. Therefore, 0.72-mm-thick sheet exhibits poor formability. The grain size of the 1.20-mm-thick sheet is finer than other two sheets. Due to this reason the sheet of 1.20 mm thickness shows higher $\bar{r}$ value. The steel with high $\bar{r}$ resists thinning in the thickness direction and exhibits better formability [13].

Tensile properties

The average strain hardening exponent ($\bar{n}$) value indicates stretchability and formability [13, 14]. As the $\bar{n}$-value increases, the stretchability also increases. The 0.72-mm-thick sheet possesses comparatively less average strength coefficient value ($\bar{K}$) due to presence of larger grains, whereas the grain size of 1.00-mm- and 1.20-mm-thick sheets is almost in same order and they possess higher $\bar{K}$ value. The 1.20-mm-thick steel possesses a higher value of UTS, compared to other two sheets but it possesses a low yield stress, compared to other two sheets (Tables 3 and 4).

Limit strains and limit stresses

The forming and fracture limit diagrams of all steels are presented in Fig. 2. The forming and fracture stress limit curves for the sheets are shown in Fig. 3. The dip in the central region of the stress curve corresponds to plane strain deformation. In the right hand side of the stress curve, in the tension–compression region, the stress is more due to the accommodation of more plastic deformation, whereas the left hand side of the stress curve represents the tension–tension region, where the stress is comparatively lesser due to lesser formability. The diagonal shift of the

Table 3 Tensile properties of SPRC-35 high strength IF steel of 1.00-mm thickness

Orientation relative to rolling direction	Strain hardening exponent n	Strength coefficient K (MPa)	Yield stress (σ_y) (MPa)	Ultimate tensile stress in MPa	UTS/σ_y	%Elongation
0°	0.2760	460	143	344	2.59	34.82
45°	0.2799	520	Average	Average		
90°	0.2651	530				
Average[a]	0.2752	507.5				

[a] Average $= (X_0 + 2X_{45} + X_{90})/4$, where X is n-value or K-value

Table 4 Tensile properties of SPRC-35 high strength IF steel of 1.20-mm thickness

Orientation relative to rolling direction	Strain hardening exponent n	Strength coefficient K (MPa)	Yield Stress (σ_y) (MPa)	Ultimate Tensile stress in MPa	UTS/σ_y	%Elongation
0°	0.2524	470	140	361	3.28	38.60
45°	0.2898	680	Average	Average		
90°	0.2704	620				
Average[a]	0.2756	612.5				

[a] Average $= (X_0 + 2X_{45} + X_{90})/4$, where X is n-value or K-value

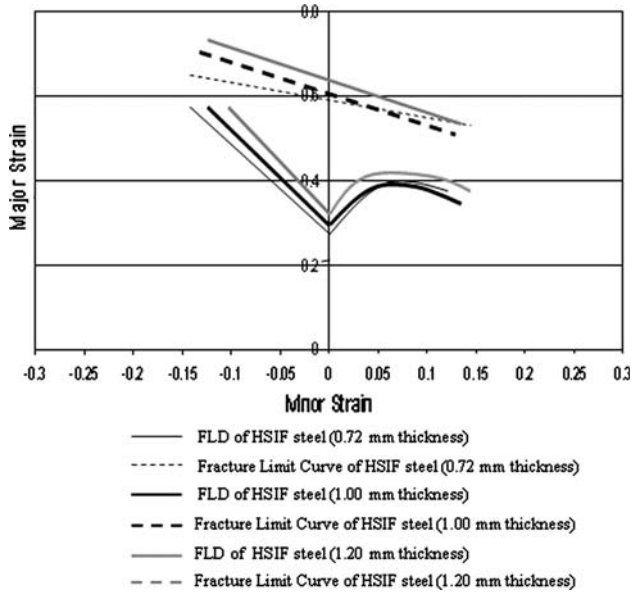

Fig. 2 Comparison of FLDs for various high strength IF steels

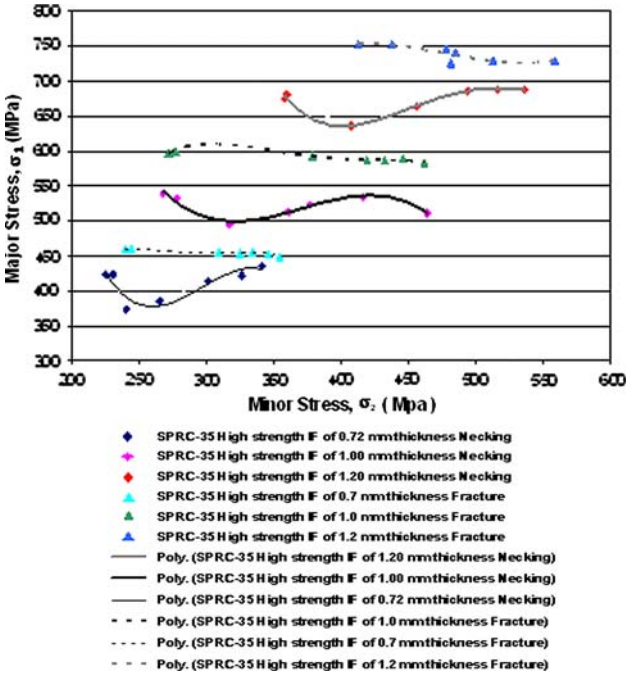

Fig. 3 Stress-based forming limit diagrams of high strength IF steels

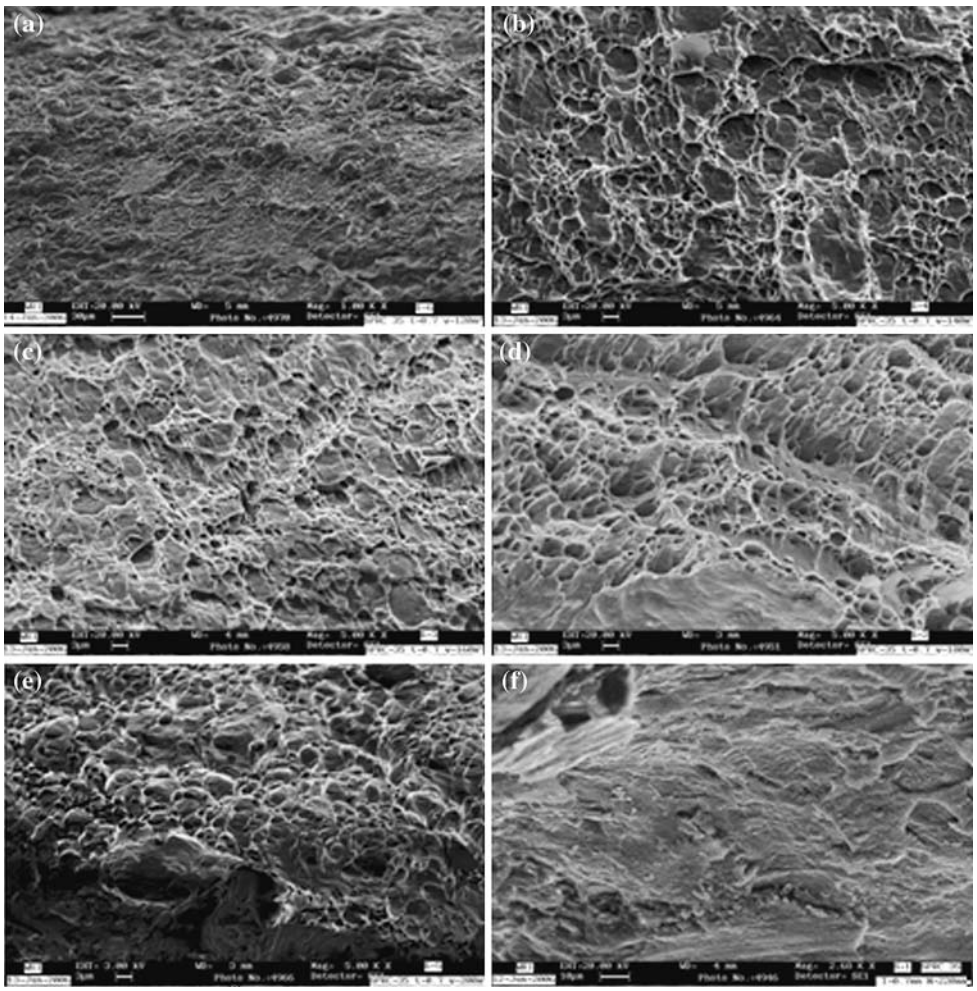

Fig. 4 SEM images taken for the fracture surfaces of high strength IF steel of 0.72-mm thickness, fracture surface for: (**a**) tension–compression condition at magnification 1000X; (**b**) plane strain condition at magnification 5000X; (**c**, **d**) tension–tension condition at magnification 5000X; (**e**) tension–tension condition at magnification 1500X; (**f**) tension–tension condition at magnification 2680X

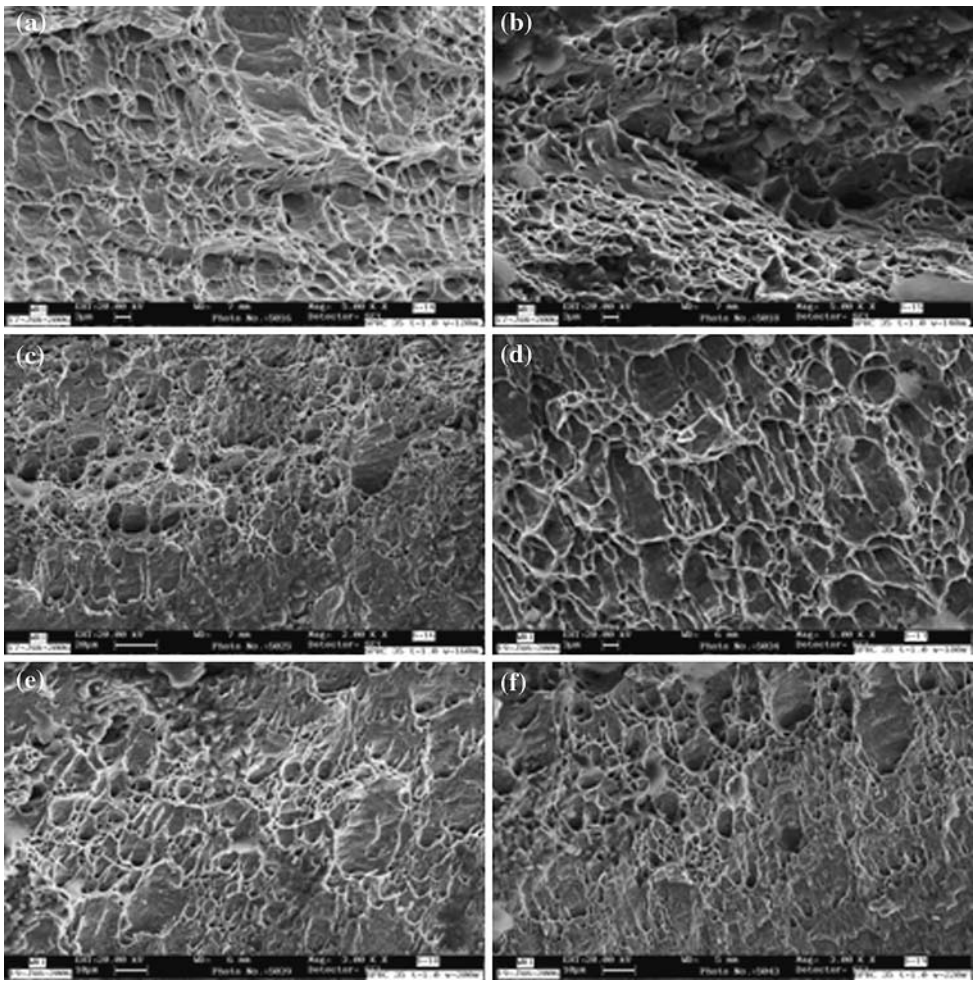

Fig. 5 SEM images taken for the fracture surfaces of high strength IF steel of 1-mm thickness, fracture surface for: (**a**) tension–compression condition at magnification 5000X; (**b**) plane strain condition at magnification 5000X; (**c**) tension–tension condition at magnification 2000X; (**d**) plane strain condition at magnification 5000X; (**e**) tension–tension condition at magnification 3000X; (**f**) tension–tension condition at magnification 3000X

forming and fracture limit stress curve of 1.20-mm-thick high strength IF steel sheet shows that it accommodates more strain and better formability. Since, the microstructure of the sheet having 1.20-mm thickness shows fine elongated ferrite grains and lesser amount of fine second phase particles, they show better formability in all regions. The steel of thickness 0.72 mm shows poor formability due to large amount of coarse carbides, apart from coarse-grained cum equiaxed microstructure. The 1.20-mm-thick sheet exhibits higher (UTS/σ_y) ratio with low yield stress, higher $(\bar{r})$ value and favourable microstructure as compared to other two sheets. Therefore, it exhibits higher formability than other two sheets and exhibits higher forming stress, fracture stress and higher gap between forming stress limit curve and fracture stress limit curve. The sheet having thickness of 0.72 mm possesses much lower limit stress values compared to other two steels due to its coarse and equiaxed microstructure with large amount of carbides. When compared to 0.72-mm-thick sheet, the 1.00-mm-thick sheet exhibits relatively fine-grained microstructure and shows a better value of percentage elongation and ratio of (UTS/σ_y).

Voids

The SEM fractography details are provided in Figs. 4–6. The shape of the voids is categorized as spherical, prolate and oblate voids. In the initial stage of research on voids, they are assumed spherical [1]. Later, it is found that the shape of the voids is taking different shapes depending on the state of stress/strain conditions. The prolate and oblate voids are elliptical in shape. The prolate voids are elongated more in the thickness direction than in the plane of the sheet and the oblate voids are elongated more in the direction of plane of the sheet. Not only the type of voids, but also the number of voids is affected by the forming conditions. Among the sheets taken for the study, the 1.2-mm-thick steel sheet shows large number of voids in the SEM images taken at its fracture surface compared to other two sheets. The presence of large number of voids is due to its higher thickness, higher strain hardening index $\bar{n}$ value and lesser number of carbide particles. As the strain hardening index $\bar{n}$ value increases, the stress required for the plastic deformation also increases and this may lead to the formation of larger number of voids due to the presence of lesser carbide particles and fine sulphides.

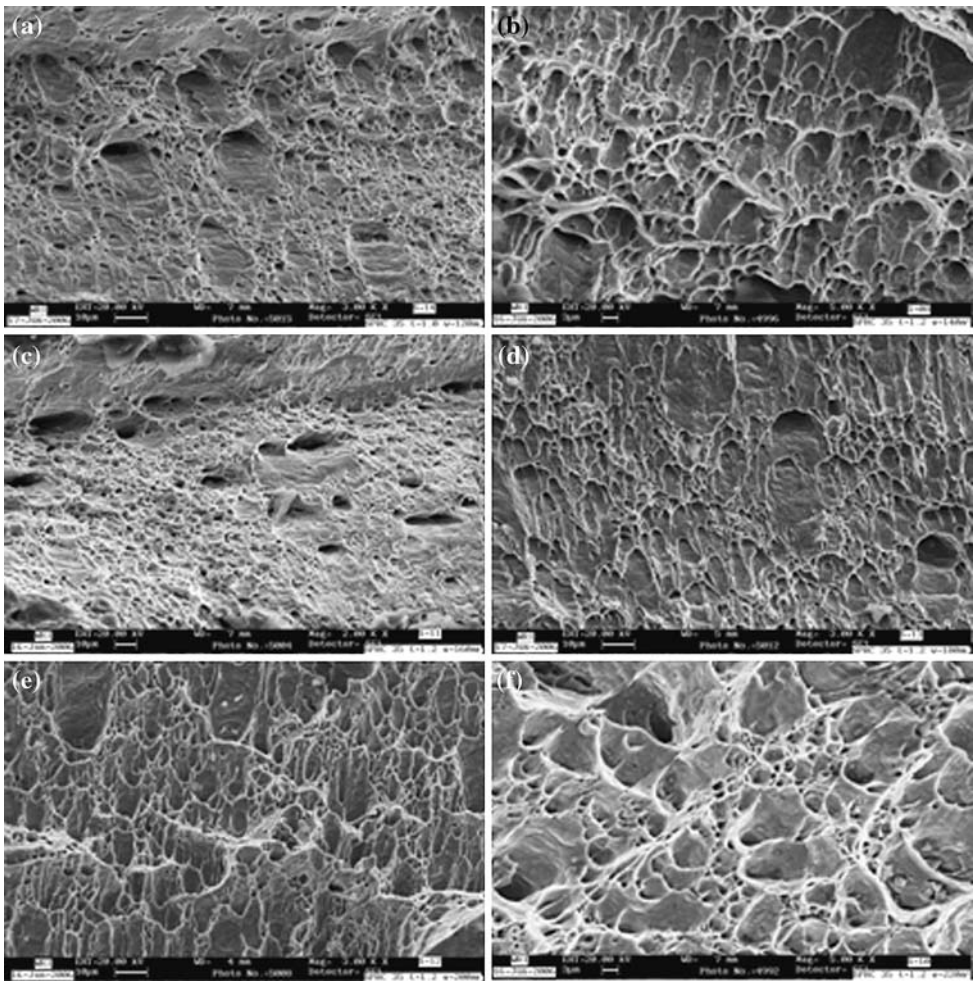

Fig. 6 SEM images taken for the fracture surfaces of high strength IF steel of 1.20-mm thickness, fracture surface for: (**a**) tension–compression condition at magnification 5000X; (**b**) plane strain condition at magnification 5000X; (**c**) tension–tension condition at magnification 2000X; (**d**) tension–tension condition at magnification 3000X; (**e**, **f**) tension–tension condition at magnification 3000X

In other two sheets, the number of voids is lesser compared to 1.2-mm-thick sheet. It is also noticed that the voids are almost spherical in the case of the blanks of width 200 mm which is subjected to nearly equibiaxial strain condition. This is due to the reason that the major strain and minor strain are tensile in nature, they are acting in the plane of the surface of the sheet and the thickness strain is found to be lesser at fracture. In tension–compression strain condition, the minor strain (in the width direction) is less and therefore it shows the a large number of prolate voids. It is also true that the orientation of second phase particle influence the formation of both prolate and oblate voids. The SEM images of all the sheets considered for the study show more number of prolate voids because their microstructures show that second phase particles are parallel to the thickness direction of the sheet. These voids are formed around the second phase particle due to the mismatch of these second phase particles and the metal matrix, whereas in tension–tension strain condition, the voids are developed at the fracture of second phase particles and therefore they are in spherical shape.

Figure 7 shows the spatial distribution of voids, ligament thickness, RMA and void area. Figure 8 is plotted between

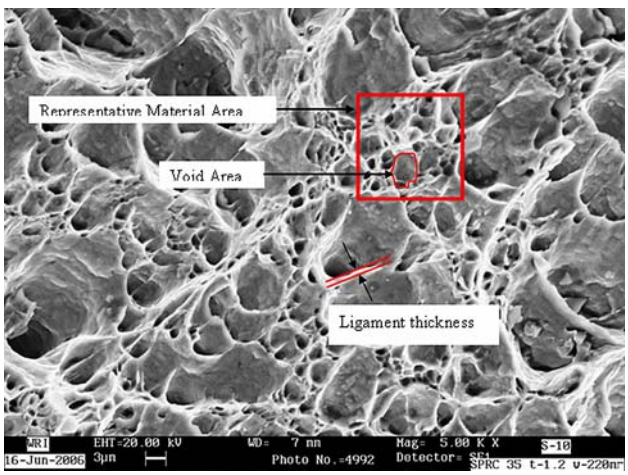

Fig. 7 Fractography showing spatial distribution of voids

the strain triaxiality factor (which is the ratio between hydrostatic strain and effective strain) and d-factor. From this figure, it is known that the effective strain increases as the void size decreases. Therefore it can be concluded that as the strain triaxiality factor increases the d-factor also

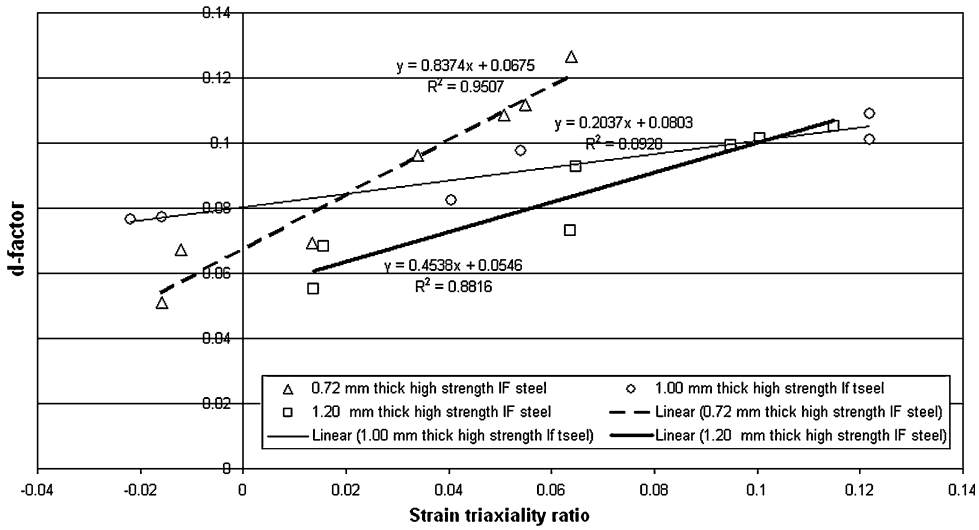

Fig. 8 d-factor versus strain triaxiality factor (T_o) for high strength IF steels

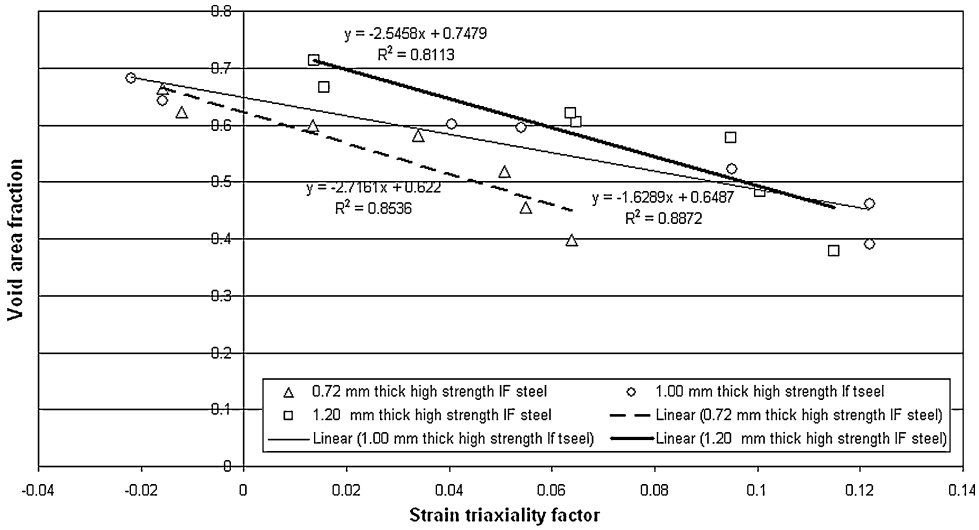

Fig. 9 Void area fraction (V_a) versus strain triaxiality factor for high strength IF steels

increases. The 1.2-mm-thick sheet shows lower slope value and therefore this sheet exhibits better formability. This slope is lowest for 1.00-mm-thick sheet because it contains spherical sulphide particles in the microstructure. (Because this steel contains more amounts of S and Mn)

The strain triaxiality factor is responsible for the initiation of void and hydrostatic strain is responsible for the growth of the void. Therefore, these two parameters have some impact on the void area fraction as well as on the formability. It shows that the fracture occurs when this void area fraction reaches a critical value for steels and for any given condition. This critical value also depends on the thickness of the sheet. The nature of variation of void area fraction with respect to strain triaxiality factor shows the similar pattern but with different slope values as shown in Fig. 9. It is further noticed from the curve fitting results and its correlation coefficient that the hydrostatic strain influence the void area fraction to a greater extent compared to the strain triaxiality factor.

The hydrostatic stress and the stress triaxiality factor are directly proportional to hydrostatic strain and strain triaxiality factors. Hence, the influence of hydrostatic stress and the stress triaxiality factor on d-factor, δd-factor and void area fraction are assumed to be similar to that of hydrostatic strain and strain triaxiality factor. The combination of lesser stress triaxiality factor (T) and higher Lode angle refers to higher severity of triaxial stress state as described elsewhere [12]. For the sheet metals subjected to tension–tension strain condition, the Lode angle is measured as a higher value and a lower value for tension–compression strain condition. The higher Lode angle refers to higher severity of triaxial stress state. Therefore the severity of triaxial stress state is high for tension–tension strain condition and this shows lesser formability compared to tension–compression strain condition in all steels. In tension–tension strain condition, the d-factor and δd- factor have a lower value due to this higher severity of triaxiality in all steels. Figure 10 shows the effect of stress triaxiality factor on the Lode angle determined.

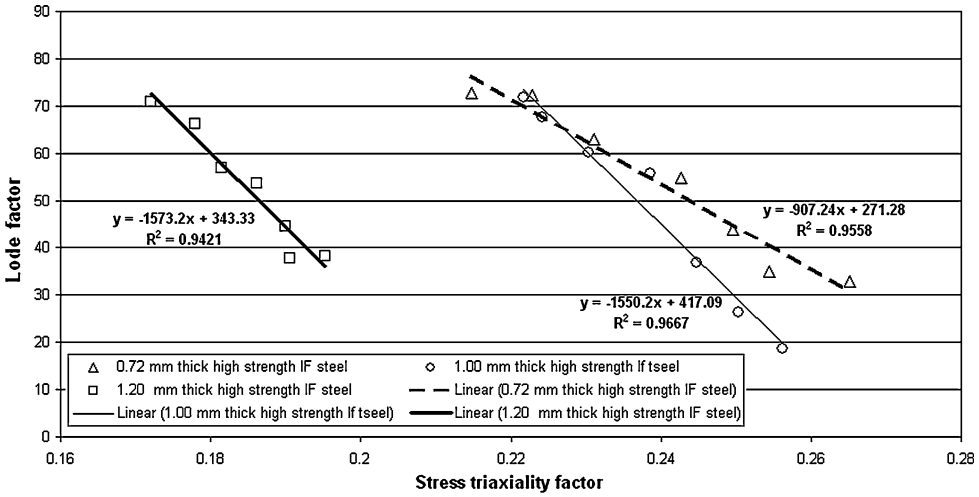

Fig. 10 Lode factor (θ) versus stress triaxiality factor (T) for high strength IF steels

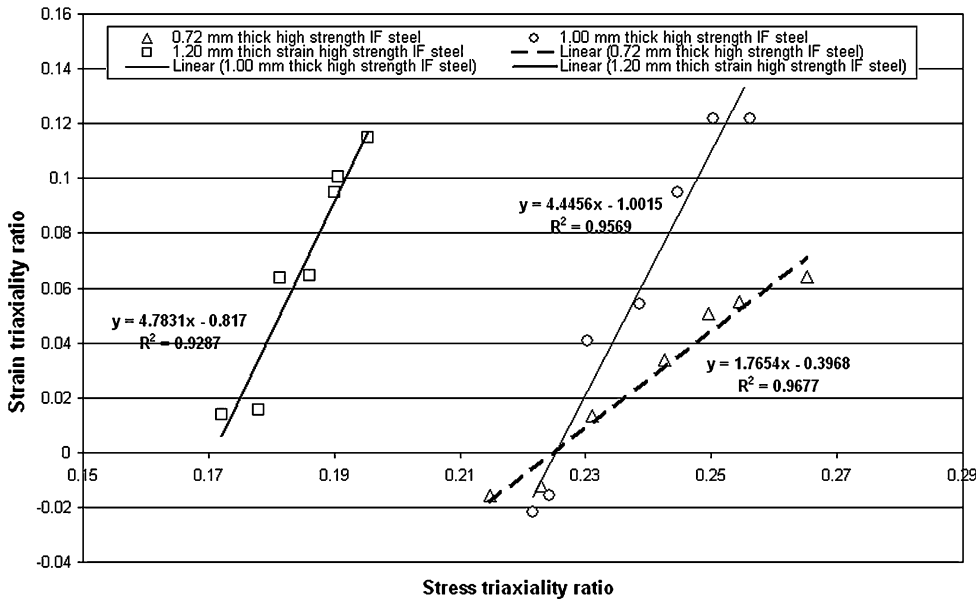

Fig. 11 Strain triaxiality factor (T_o) versus stress triaxiality factor (T) for high strength IF steel

From the curve fitting results and high correlation coefficient, it is clearly understood that the stress triaxiality factor has very good correlation with the Lode angle. From Fig. 11, it is also understood that stress triaxiality factor also has very good correlation with the strain triaxiality factor. Therefore, it can be concluded that the above studies based on strain triaxiality factor are meaningful in case of sheet metal.

The L/W ratio gradually increases from a lesser value in for tension–compression condition to a higher value for tension–tension condition and as the L/W ratio increases the proneness to fracture also increases. The 0.72-mm-thick sheet shows the highest L/W ratio compared to other steels for any given minor strain value, the 1.20-mm-thick steel shows the lowest L/W ratio and exhibits better formability, as shown in the Fig. 12. Figure 13, a plot drawn between the ratio (L/W) voids and Mohr's circle shear strain (γ_{12}), shows straight line with negative slope. Since, one of the strains is tensile in nature and the other is compressive, the tension–compression condition exhibits a larger Mohr's circle shear strain (γ_{12}). For tension–tension condition, in which both strains are tensile in nature, steels exhibit a lower (L/W) ratio of voids.

As shown in Fig. 14, a plot drawn between the ratio (L/W) of voids and the shear strain (γ_{23}), the shear strain (γ_{23}) measured is the lowest in tension–tension region and the (L/W) ratio of voids is larger for the 0.72-mm-thick sheet compared with other two steels. The highest slope of the plot in the case of 0.72-mm-thick sheet and lowest slope in 1.20-mm-thick sheet due to their microstructure and mechanical properties. In Fig. 15, plots between the (L/W) ratio of the voids and Mohr's circle shear strain (γ_{13}) show negative slope value for all the sheets, the range of γ_{13} is higher for 1.20-mm-thick sheet which represents higher formability, compared to other two sheets. As the strain ratio, ($\varepsilon_m/\varepsilon_e$) increases the

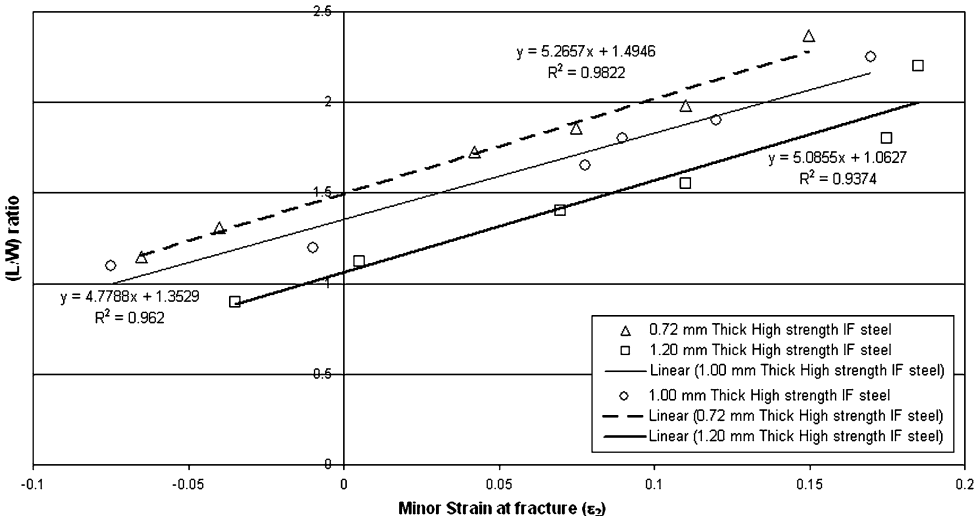

Fig. 12 (L/W) ratio of voids versus minor strain (ε_2) at fracture for high strength IF steel sheets

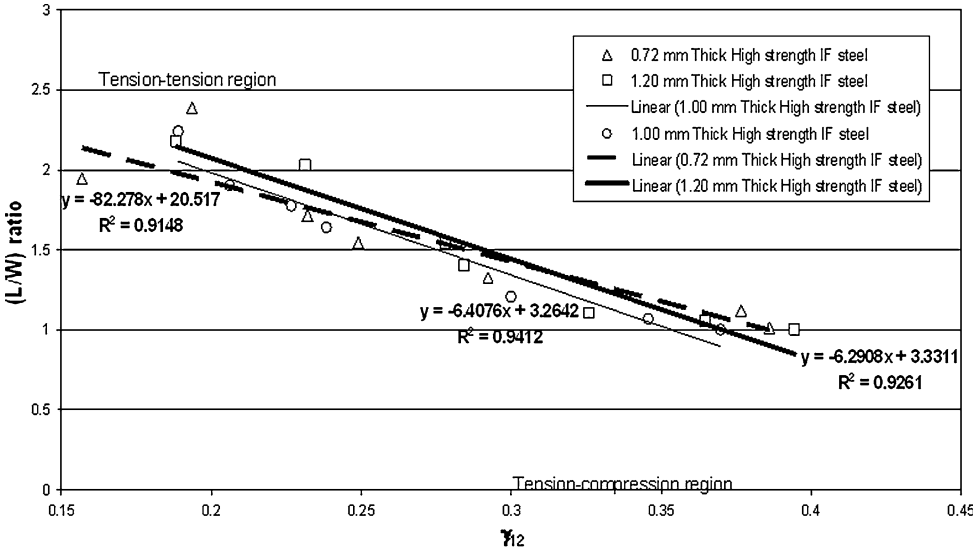

Fig. 13 (L/W) ratio of voids versus γ_{12} or high strength IF steel sheets

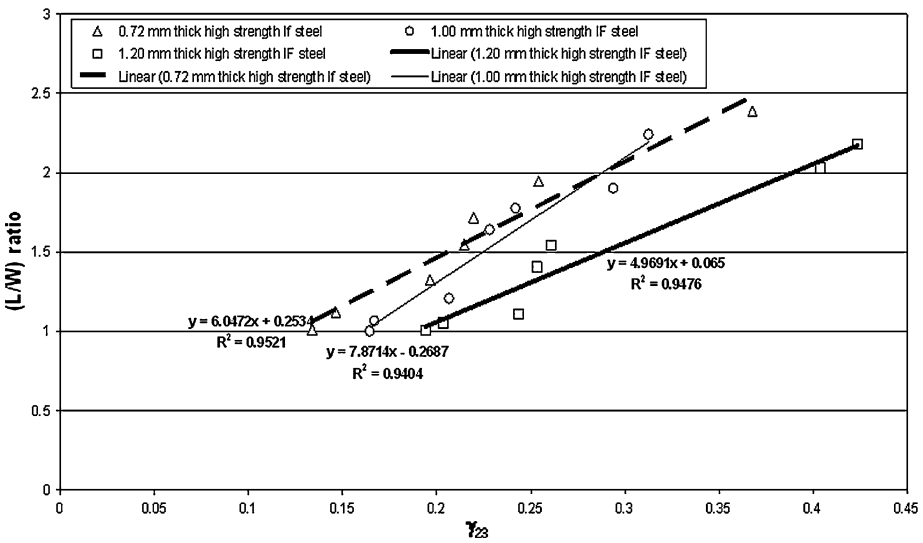

Fig. 14 (L/W) ratio of voids versus γ_{23} or high strength IF steel sheets

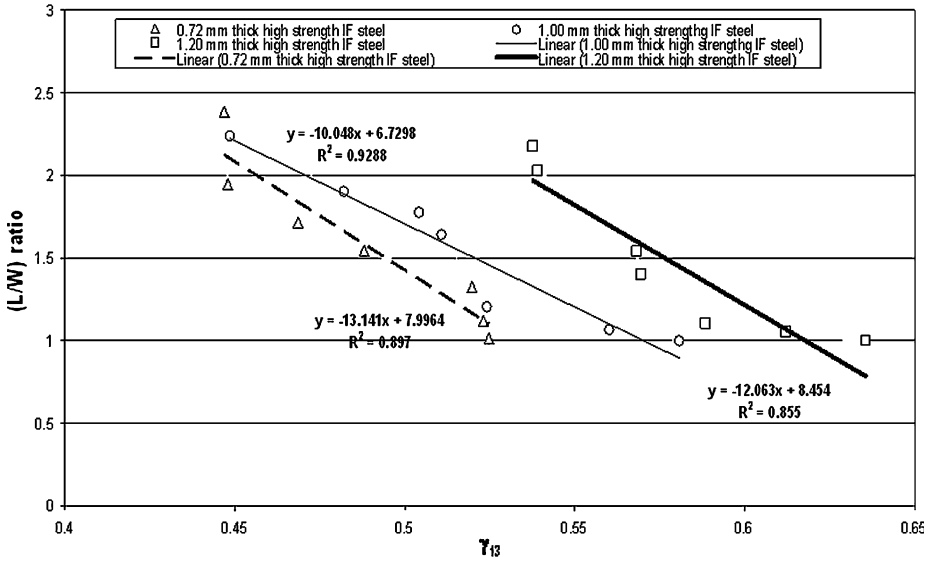

Fig. 15 (L/W) ratio of voids versus γ_{13} or high strength IF steel sheets

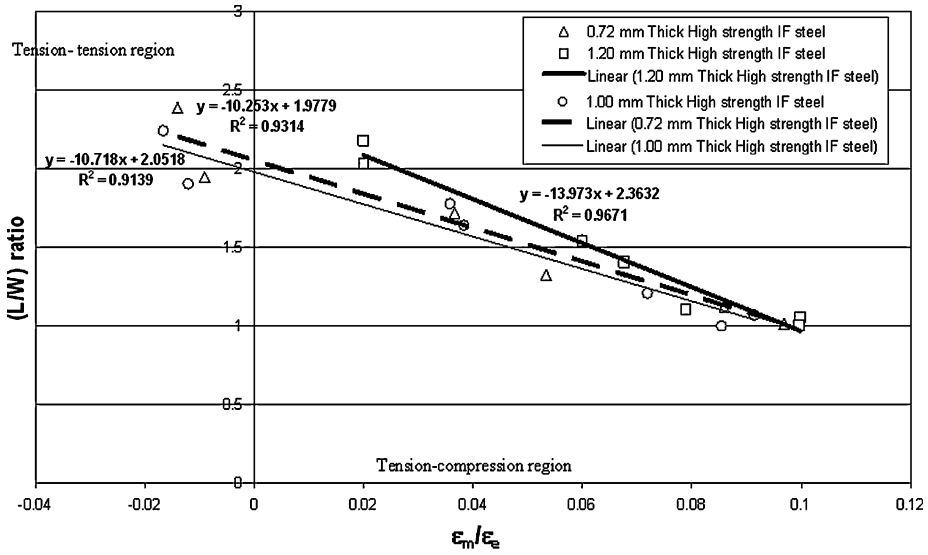

Fig. 16 (L/W) ratio of voids versus ($\varepsilon_m/\varepsilon_e$) Strain triaxiality factor (T_o) at fracture for high strength IF steel sheets

(L/W) ratio also decreases and the rate of decrease in (L/W) ratio is higher for 0.72-mm-thick sheet due to its microstructure, compared to other two steels as shown in Fig. 16.

Conclusion

Following conclusions can be drawn from the above results and discussion. The steel sheets having higher stain hardening index ($\bar{n}$) value counteracts void growth and coalescence. The steel sheets having lower d-factor show better formability. The high strength IF steel sheet having thickness of 1.20 mm exhibits higher formability and fracture strain due to its high $\bar{n}$-value, $\bar{r}$-value and presence of fine second phase particles. The hydrostatic strain or mean strain (ε_m) shows better correlation with d- and δd-factors. Specifically, δd-factor is found to be greater for 1.20-mm-thick high strength IF steel sheet possessing fewer and finer amounts of second phase particles and due to this reason, 1.20-mm-thick steel sheet shows better formability and fracture strain. The Hydrostatic strain (ε_m) also influences the void area fraction (V_a) to great extent. The Void area fraction (V_a) is found to be larger for 1.20-mm-thick high strength IF steel sheet due to the presence of lesser amount of carbides and sulphides and thus exhibits better formability and fracture strain than the rest of the sheets. The higher Lode angle and lesser stress triaxiality factors for 1.20-mm-thick high strength IF steel sheet are due to the presence of lesser amount of second phase particles. In addition to that, 1.20-mm-thick steel sheet shows lower L/W ratio and exhibits better formability and fracture strain. There is a better correlation between stress triaxiality factor and Lode angle.

Appendix 1

Mean stress (σ_m) calculation

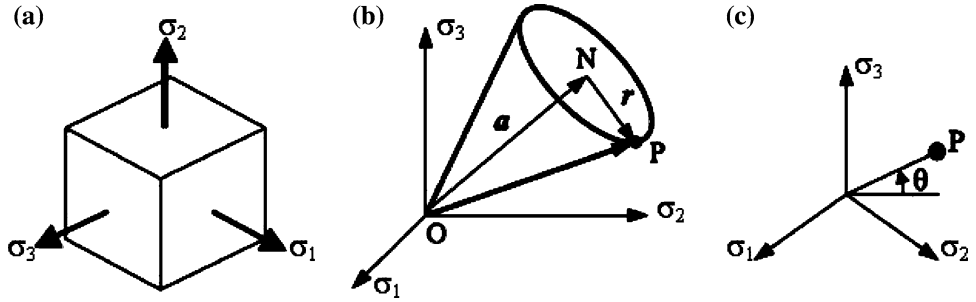

As explained elsewhere [12], let σ_1, σ_2 and σ_3 be the principal stresses and introduce the (σ_1, σ_2, σ_3) coordinate system. In Fig. (b), consider a line ON passing through the origin and having equal angles with the coordinate axes. Then every point on this line corresponds to a mean stress state. The plane passing through the origin and perpendicular on ON is called π plane. Consider an arbitrary stress state at point P with stress components σ_1, σ_2 and σ_3. The stress vector $\vec{OP}$ can be decomposed into two components, the component $\vec{a}$ parallel to ON and the component $\vec{r}$ perpendicular to ON, where

$$a = \sqrt{3}\,(\sigma_m) \quad \text{and} \quad r = \sqrt{2/3}(\sigma_e)$$

Effective stress (σ_e) calculation

The effective stress (σ_e) is given as follows.

$$\sigma_e^2 = \sigma_1^2 - (2/C)\sigma_1\sigma_2 + (B/C)\sigma_2^2$$

where σ_1 = major stress; σ_2 = minor stress; $B = (1 + r_{90})/r_{90}$; $C = (1 + r_0)/r_0$

Equation 1 can be simplified as follows by substituting m

$$\sigma_e = [1 - (2/C)(1/m) + (B/C)(1/m^2)]^{0.5}\sigma_1$$

where

$$m = (\sigma_1/\sigma_2) = (Bl + 1)/(l + C) \text{ and } l = (\varepsilon_1/\varepsilon_2)$$

where σ_m and σ_e represent the mean stress and the effective stress, respectively. Consequently, the stress triaxiality factor is

$$T = (\sigma_m)/(\sigma_e) = (\sqrt{2}/3)\frac{a}{r}$$

Lode's factor calculation

Lode's factor is calculated from the strain calculations. In Fig. (c), the angles between the projections of the coordinate axes ε_1, ε_2 and ε_3 on the π plane are 120°. Let θ be the angle measured from the horizontal axis, then

$$\tan\theta = \frac{[2\varepsilon_3 - \varepsilon_2 - \varepsilon_1]}{\sqrt{3}(\varepsilon_2 - \varepsilon_1)}$$

Effective strain (ε_e) and mean strain (ε_m) calculation

The effective strain is calculated using the following equation.

$$\text{Effective strain } (\varepsilon_e) = \frac{2}{3(2 + R_d^2)}\left\{\left[(\varepsilon_1 - \varepsilon_2)^2 + (\varepsilon_2 - \varepsilon_3)^2 + (\varepsilon_3 - \varepsilon_1)^2\right] + \left[\frac{(\varepsilon_1 + \varepsilon_2 + \varepsilon_3)^2}{3}\right](1 - R_d^2)\right\}^{1/2}$$

$$\text{Mean strain}(\varepsilon_m) = \frac{(\varepsilon_1 + \varepsilon_2 + \varepsilon_3)}{3}$$

where R_d is the relative density of the formed and fractured sheet sample used for SEM and ε_1 is the major strain, ε_2 is the minor strain, ε_3 is the thickness strain.

Strain triaxiality factor (T_o) is calculated by

$$T_o = (\varepsilon_m)/(\varepsilon_e)$$

Mohr's circles shear strain calculation

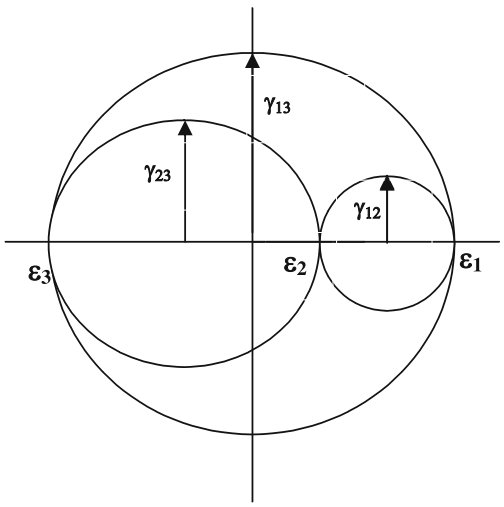

Mohr's Circles for Shear Strain

ε_1 is the major strain, ε_2 is the minor strain, ε_3 is the thickness strain,

Mohr's circle shear strain $\gamma_{12} = (\varepsilon_1 - \varepsilon_2)/2$

Mohr's circle shear strain $\gamma_{23} = (\varepsilon_2 - \varepsilon_3)/2$

Mohr's circle shear strain $\gamma_{13} = (\varepsilon_1 - \varepsilon_3)/2$

Mean strain $\varepsilon_m = (\varepsilon_1 + \varepsilon_2 + \varepsilon_3)/3$

Note: ε_3 (thickness strain) is always compressive in nature. Therefore, the ε_3 values are substituted as negative values in the formulae. ε_1, ε_2 and ε_3 were measured in the fracture region. Since ε_1, ε_2 and ε_3 are fracture strains, volume constancy principle cannot be applied. Therefore, $\varepsilon_1 + \varepsilon_2 + \varepsilon_3 \neq 0$.

Strain ratios are derived as follows

When considering ε_1 and ε_2

(a)

$$\gamma_{12} = (\varepsilon_1 - \varepsilon_2)/2$$
$$(\gamma_{12}/\varepsilon_m) = 1/2[(\varepsilon_1/\varepsilon_m) - (\varepsilon_2/\varepsilon_m)]$$

When considering ε_1 and ε_3

(b)

$$\gamma_{13} = (\varepsilon_1 + \varepsilon_3)/2$$
$$(\gamma_{13}/\varepsilon_m) = 1/2[(\varepsilon_1/\varepsilon_m) + (\varepsilon_3/\varepsilon_m)]$$

When considering ε_2 and ε_3

(c)

$$\gamma_{23} = (\varepsilon_2 + \varepsilon_3)/2$$
$$(\gamma_{23}/\varepsilon_m) = 1/2[(\varepsilon_2/\varepsilon_m) + (\varepsilon_3/\varepsilon_m)]$$

References

1. Tvergaard V (1981) Int J Frac 17:389
2. Needleman A, Tvergaard V (1987) J Mech Phys Solids 35:151
3. Gologanu M, Leblond JB, Bevaux J (1993) J Mech Phys Solids 41:1723
4. Gologanu M, Leblond JB, Bevaux J (1994) J Eng Mater Tech Solids 116:290
5. Gologanu M, Leblond JB, Bevaux J (1995) In: Suquet P (ed) Continuum mcromechanics. Springer-Verlag, Berlin
6. Benzerga AA, Bessson J, Pianeau A (1999) J Engg Mater Technol 121:221
7. Pardoen T, Hutchinson JW (2000) J Mech Phys Solids 48:2467
8. Benzerga AA, Bessson J, Pianeau A (2004) Acta Mater 52:4639
9. Kim J, Gao X (2005) Int J Solids Struct 42:103
10. Kim J, Gao X, Srivatsan TS (2003) Int J Solids Struct 40:7357
11. Gao X, Wang T, Kim J (2005) Int J Solids Struct 42:5097
12. Gao X, Kim J (2006) Int J Solids Struct 43:6277
13. Stoughton TB (2000) Int J Mech Sci 42(1):1
14. Narayanasamy R, Sathiya Narayanan C (2006) Mater Sci Eng A 417:197
15. Graf AF, Hosford WF (1993) Metall Trans A 24(3):2497